J. Fluid Mech. (1999), *vol.* 397, *pp.* 231–258. Printed in the United Kingdom

Self-similarity, momentum scaling and Reynolds stress in non-premixed turbulent spray flames

By A. N. KARPETIS AND A. GOMEZ

Yale Center for Combustion Studies, Department of Mechanical Engineering, Yale University, New Haven, CT 06520, USA

(Received 13 February 1998 and in revised form 24 May 1999)

An experimental study was conducted in a turbulent spray flame in which droplets were produced ultrasonically at low velocity relative to the host gas. In this fashion, injector-specific effects on the two-phase flow were minimized and a scenario generally characteristic of the far field of practical spray systems could be simulated. Close to the burner exit, the spray flame appeared as a dense column of drops burning with an envelope flame. Further downstream, it opened up slowly in the radial direction and developed a turbulent 'brush' appearance. Measurements of the size, velocity and concentration of the droplets, and of gas-phase velocity and temperature were made by combining a Phase-Doppler interferometric technique with Stokes/anti-Stokes Raman thermometry. The experimental data were used to derive scaling and self-similarity for the Reynolds-averaged continuity and momentum equations using suitable transformations.

Results showed three distinct regions, on the basis of the behaviour of the gas axial velocity in the spray flame. In the lower part of the flame, the gas momentum increased because of vaporization. In the intermediate region of the spray flame, the axial velocity decayed along the centreline as an inverse power of the distance from the virtual origin, with exponents smaller than unity. In the upper part of the spray flame, the flow field recovered the axial velocity decay that is typical of incompressible jets, namely as an inverse of the axial distance. Self-similar behaviour held for the axial velocity throughout the intermediate region. The vapour source term in the gas continuity equation scaled approximately as an inverse power of axial distance, and exhibited self-similarity throughout the spray flame. As a result, a simple model of the Reynolds stress term could be formulated, in which two competing contributions appear: one, that is due to turbulent transport, tends to increase the value of the velocity correlation; another, that is due to the vaporization term, tends to reduce the value of the velocity correlation and can be construed as a vaporization-induced tendency towards relaminarization. The first term is modelled by a classic gradient-transport approach yielding an empirical mixing length relating the velocity correlation to the average velocity gradient. Model and experiments are found to be in good agreement, especially sufficiently far from the injector, where one-way coupling between the two phases holds.

1. Introduction

Spray combustion is an important facet of modern technology. It is used in jet engine combustors, industrial and residential furnaces, internal combustion engines, to

name but a few of the applications that utilize combusting sprays as primary energy source. Invariably in all of these applications, the combustion can be considered turbulent. The use of spray burning in most non-premixed combustion environments can have a profound influence on flame structure and pollutant formation. Despite its technological importance, the subject has been insufficiently studied at a fundamental level, probably because of its inherent complexity.

For the past forty years the research community has focused on a much more manageable liquid fuel system, the classic single-droplet burning, that was originally regarded as the building block of spray combustion (Williams 1985). Experiments of this kind can be conducted under well-defined and well-controlled conditions. Modelling can even account for detailed kinetics and transport for combustion of multi-component droplets (Marchese *et al.* 1996). But, the relevance of single-droplet burning to practical spray systems is limited. Droplets are known to evaporate and burn as a group, interacting with one another in practical environments (Chigier & McCreath 1974).

We have been pursuing the objective of bridging the gap between classical single-droplet burning studies and practical spray flames by using some well-defined configurations, encompassing at first laminar spray diffusion flames. The laminar configurations include counterflow (Chen & Gomez 1992) and co-flow (Chen & Gomez 1996, 1997). The experimental systems are simple and amenable to detailed numerical modelling (Gao *et al.* 1996). Droplet–droplet and droplet–flame interactions can be studied in the absence of turbulence complications. As a natural development in this effort to understand fundamental features of practical spray systems, we now face the much more challenging case of turbulent spray flames.

We will concentrate on an axisymmetric configuration, which is the one most often found in practice. In this case, it is conceptually useful to think of both turbulent gaseous jet diffusion flames and spray flames as complex 'variations' on the theme of turbulent jets. In increasing order of complexity, a jet diffusion flame differs from a turbulent jet because of the presence of a distributed source of energy due to combustion. While certainly related to the gaseous jet non-premixed analogue, a spray flame differs because of the presence of drops acting as distributed sources of mass, as well as sources/sinks of momentum.

Drop dispersion and collective drop vaporization and burning are important physical mechanisms in spray flames. A number of studies have concentrated on either one of these issues, as in particle-laden jet studies addressing the former (e.g. Longmire & Eaton 1992) and group combustion models addressing the latter (e.g. Labowsky & Rosner 1978). As a result, they fail to capture the full picture of spray combustion: particle-laden jets lack the effect of the combustion heat release, while group combustion models, in view of their prototypical, spherical geometry configuration, miss the important convective–diffusive nature of the full problem.

The challenge to experimentation posed by turbulent spray flames stems from two difficulties associated with the liquid phase, in addition to the obstacles customarily dealt with in turbulent gaseous flames. First, spray combustion is implemented in everyday practice with a strong influence on the combusting flow field of the fuel injector used to disperse the liquid. It is not uncommon for droplets to be injected at relative velocities on the order of hundreds of metres per second with respect to the gaseous phase (Kamimoto & Koyabashi 1991). As a result, the drop motion, especially close to the injector, and in some practical cases throughout the combustion field, is influenced by specific aspects of the injector design. Liquid atomization and gas flow in the combustion chamber are very strongly coupled and the atomization in itself

induces turbulence. Thus, the gas phase is also strongly affected by the injector design. This, in turn, diminishes the 'universality' of any results that might be obtained from such a spray flame.

The second difficulty originates from the hostility of this environment that all but precludes quantitative experimentation. Laser interferometric techniques have already been extensively used in such environments for the characterization of the dispersed phase, as is also the case for the present study. On the other hand, laser spectroscopic techniques, that are virtually irreplaceable for temperature and species measurements in a turbulent environment, have been adapted only very recently to combusting sprays (Takahashi *et al.* 1996; Luczak *et al.* 1996), in some case through developments in our own laboratory (Karpetis & Gomez 1996). Consequently, this is the first study in which both types of diagnostic techniques, specifically Phase Doppler interferometry and spontaneous Raman scattering thermometry, are applied quantitatively in the same spray combustion system.

As regards the first difficulty, the influence of the fuel injector, we chose to bypass it altogether in an effort to establish general features of combusting sprays. To that end, droplets are generated with a gentle atomization technique, which produces minimal velocity slip between the two phases. In this manner we avoid effects on the structure of the spray flame that are specific to the particular injector or, equivalently, the initial and boundary conditions of the dispersed phase. Turbulence in the oxidizer stream is 'synthesized' independently by the combination of a perforated plate and a contoured flow passage. Since the role of the initial conditions is minimized on purpose, this study can provide information that is relevant only to the far-field region of practical spray flames, in which the droplets, at least in an average sense, are equilibrated with the gaseous stream.

The experimental methods and results will be discussed first. Subsequently, vapour source and momentum self-similarity will be established in the spray flames and the effect of these scaling laws on the Reynolds stress will be examined. Based on the experimental measurements, an algebraic model for the Reynolds stress will be presented. This type of information should be useful to engineering models of turbulence or to submodels of more complex approaches.

2. Experimental methods

The burner used in this study is shown in figure 1. It was designed with two objectives: (*a*) to maximize the level of gas turbulence, in view of the inevitable relaminarizing effect of the high combustion temperatures and (*b*) to minimize the effect of the drop initial conditions, so that most of the drops would respond to at least the average gas velocity. The resulting spray would resemble a line source of vapour, with drops convected along the axial direction, while diffusing in the radial direction under the action of gas turbulence.

The liquid fuel was injected using a commercial ultrasonic nebulizer (Sonotek). This device can disperse modest liquid flow rates, while imparting minimal velocity to the liquid drops. The drops were carried upwards by air fed through a series of holes arranged along the outer periphery of a plate mounted in the burner housing, as shown in figure 1. The positioning of the air inlet into the burner housing was optimized to achieve maximum turbulence levels as well as drop dispersion at the exit. By trial-and-error we arrived at a set-up very similar to the one used by other investigators (e.g. O'Young & Bilger 1997). The small initial velocities of the drops

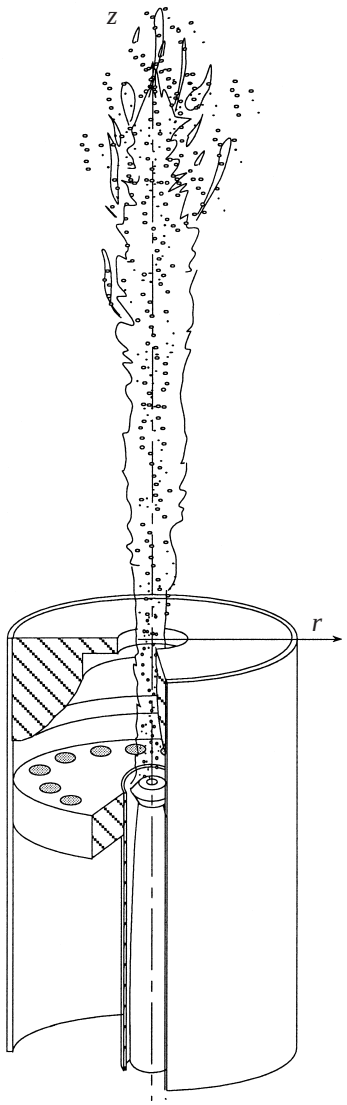

FIGURE 1. Burner and spray flame schematic.

resulted in minimal slip between the drops and the gas close to the atomizer tip†. A flame, once ignited, was anchored at the atomizer tip and extended through the contraction into the measurement field through a circular opening with diameter $D = 12.5\,\text{mm}$. The close anchoring of the flame, as observed visually through the burner opening, ensured that non-premixed combustion prevailed. The spray flame appeared as a dense column of drops burning with an envelope flame, close to the burner exit. Further up, the flame opened up slowly in the radial direction and ultimately developed into a turbulent 'brush' flame.

† As will be shown later, the gas jet is accelerating immediately after the burner exit, thus a velocity slip is expected to develop between the gas and the drops. However, this effect is a consequence of the dynamic behaviour of the spray, as opposed to being 'inherited' from atomizer-dependent initial conditions.

Detailed measurements were performed for two different spray flames, as follows. In one case, the volumetric flow rate of the air under standard conditions was $80\,\mathrm{l\,min^{-1}}$, and the liquid mass flow rate was $5.1\,\mathrm{g\,min^{-1}}$ (flame I). In the second case (flame II) the air flow rate was $110\,\mathrm{l\,min^{-1}}$ and the liquid mass flow rate was $3\,\mathrm{g\,min^{-1}}$. The overall equivalence ratio was calculated to be $\Phi_I = 0.35$ and $\Phi_{II} = 0.15$ respectively.

The conditions of the two flames correspond to a Reynolds number ($Re = UD/\nu$) of 21 000 for flame I and 29 000 for flame II under cold conditions. The type of injector used here produced a distribution of drop sizes centred around an average diameter of 30 μm. The Stokes number of a 30 μm drop under burning conditions can be estimated to be 0.3 for flame I and 0.7 for flame II, both calculated with respect to a global gas time scale D/U, where U is the average exit velocity. At the same hot conditions, the Stokes number with respect to an estimated Kolmogorov time scale would be 5 for flame I and 13 for flame II. It should be noted that these values are representative of the highest values that can be obtained in the spray flame. The above numbers were calculated using as stopping time for the droplets $\tau_d = \rho_l d^2/18\mu$, where ρ_l is the liquid density and d the droplet size under consideration. Contrary to the case of practical injectors that impart very large velocities to the liquid drops, and create large velocity slip between the drops and the gas (Kamimoto & Koyabashi 1991), the Stokes numbers achieved in the present study are sufficiently small so that any severe influence of the drop initial conditions on the spray flame behaviour can be ruled out.

Two diagnostic techniques were used in the present study. Phase Doppler Anemometry (PDA) provided single-point statistics on droplet velocity and size. We used a two-colour PDA instrument (Dantec Measurement), capable of measuring velocities and velocity correlations in two directions (r and z). By employing size discrimination, the velocity and correlation statistics of the gas in the turbulent spray flame could be derived. In principle, when enough statistics are collected, quantities related to velocity can be determined with accuracy better than 5%. The number density, mass fluxes and the drop size statistics of the liquid phase were also calculated at several locations within the spray flame. In order to determine number density and mass flux, one must first determine the laser probe volume of the PDA instrument. Since this probe volume depends on droplet size, laser power, as well as a number of other optical parameters, the best accuracy one can claim for these two derived quantities is approximately 30%. To the extent possible, all diagnostic parameters were kept constant between experiments, so as to ensure that the derived quantities were self-consistent and any error would be systematic throughout the measurement field. Since the PDA technique is susceptible to velocity bias, i.e. to over-counting the statistics of the faster drops, a transit-time weighing scheme was implemented to counteract this effect (McLaughlin & Tiederman 1973). As a result, all the velocities and correlations that will be reported here can be regarded as volume-averaged quantities, in contrast to the raw measurements which are flux-averaged quantities. It is the former that are suitable for comparison with field theories.

In order to measure the gas temperature, spontaneous Raman spectroscopy was implemented in the spray flame, details of which have been presented elsewhere (Karpetis & Gomez 1996). The technique is an application of the classic Raman spectroscopy in an environment that is particularly hostile to spectroscopic investigations. In addition to the gas temperature, it is capable of measuring the nitrogen molar fraction, despite the high droplet number densities prevailing in some areas of the spray. This study is one of the first quantitative applications of this spectroscopic method in such an environment. A schematic of the Raman thermometry system is shown in figure 2. It consists of a pulsed Nd : YAG laser, frequency-doubled to

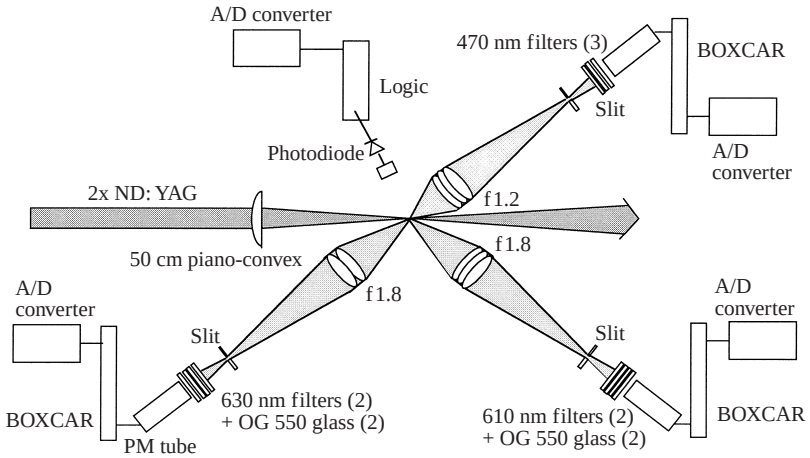

FIGURE 2. Optical configuration for Raman spectroscopy.

532 nm. The Raman (vibrational–rotational) signal of nitrogen is monitored in two spectral windows, one corresponding to the red-shifted, Stokes radiation (at 607 nm) and one corresponding to the blue-shifted anti-Stokes radiation (at 473 nm). The only difference between the system employed in this study and the one in Karpetis & Gomez (1996) is the use of a third optical channel that performs measurements (at 630 nm) of the fluorescence from potentially interfering chemical species (e.g. polycyclic aromatic hydrocarbons). This form of spectral baseline subtraction corrects the Stokes signal measured by the Raman system. The choice of methanol as the fuel was dictated by the need to avoid soot interferences in the flame (Eckbreth 1988). The probe volume was an hyperboloid with a diameter of 500 μm and an effective length of 500 μm, as created by slits in the imaging optical channels.

The smallness of the probe volume and the simplicity of the data reduction process are the main advantages of the spontaneous Raman spectroscopy, when compared to other spectroscopic techniques. The accuracy of the measurement is set by the photon statistics of the Raman signals and is determined during the calibration of the thermometry. In the present study the temperature accuracy was $\pm$ 100 K. The average temperature was determined with varied accuracy, depending on the local concentration of droplets and hence the position of the measurement. The difficulty stemmed from the fact that the high laser flux necessary to produce detectable Raman signals led to laser-induced breakdown whenever a droplet transited the measurement probe volume (Chang *et al.* 1988). This phenomenon, in turn, resulted in high light levels that consistently swamped the Raman signals. Whenever that occurred, an additional optical system was used to invalidate the particular measurement (Karpetis & Gomez 1996). As a result, this diagnostic technique measures the temperature of the gas phase, conditioned on the absence of droplets in the probe volume. Typically, an average of 600 measurements was performed at each spatial position within the spray flame. Close to the centreline and at the burner exit, where high droplet number densities prevailed, an average of only 100 temperature measurements was realizable. It should be mentioned that, because of the high rejection rate in the dense areas of the spray, and the low repetition rate of 10 Hz maintained by the pulsed laser, roughly one hour of measurements was needed in order to produce these 100 valid data. Although the Raman technique can provide the probability density function of temperature in the spray flame, we shall use only the average values in this study.

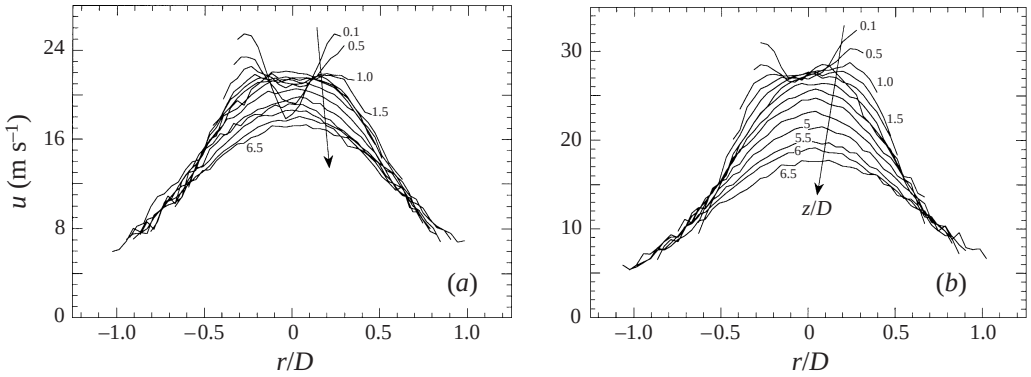

FIGURE 3. Radial scans of the average axial gas velocity in spray flames I (*a*) and II (*b*).

3. Experimental results

The results of the experimental techniques are shown in 'primitive' variable form in figures 3 to 6. In each figure, (*a*) corresponds to the measurements in flame I and (*b*) to those in flame II. Only those results that will be used subsequently are shown, namely average gas axial velocity $\overline{u}$, temperature $\overline{T}$, velocity correlations $\overline{u'v'}$, and droplet number density n. The radial coordinate is non-dimensionalized with respect to the burner diameter. The gas velocity statistics were calculated by considering all drops smaller than 8 μm as tracers and taking their average velocity to be that of the gas. Such an approach is justifiable, if one considers that the Stokes number of an 8 μm drop with respect to the estimated Kolmogorov time scale is 0.33, and that is the highest possible value under hot conditions. According to this size discrimination scheme, there is an incentive to increase this size cut-off as much as possible, in order to increase the tracer population. For a fixed duration of measurement in any location within the spray, this amounts to a larger statistical sample and hence smaller errors in the measurement. In practice, changing the above cut-off to either 6 or 12 μm yielded minimal differences for the velocity and the velocity correlations attributed to the gas phase.

Measurements were performed at $z = 0.1D$, $z = 0.5D$ and at every half a burner diameter (D) thereafter up to $z = 6.5D$. At each axial location, radial scans were performed at 500 μm intervals for both experimental techniques, PDA and Raman, but each technique was applied separately. The outermost radial position reached with the PDA technique was limited by the availability of the small drops that are used as gas tracers, while for the Raman measurements we tried to reach as close a temperature to ambient as possible. It should be mentioned that the lowest temperature that can be detected with accuracy by the Raman thermometry is 500–600 K (Karpetis & Gomez 1996). All 14 radial scans from both flames are plotted together in each of the figures 3 to 6, with arrows denoting the progression to larger axial distance, and, wherever possible, with labels denoting the non-dimensional axial location.

The axial velocity profiles show the characteristic bell-shape that is typical of jets, with values that are decreasing in the upper part of the flame due to entrainment from the ambient. Exceptions to this pattern are the radial scans close to the burner exit, exhibiting a marked depression near the centreline. The high liquid mass close to the injector causes a loss of momentum from the gas to the drops, with a wake-like effect appearing at the burner exit. As will become clear when we discuss figure 10 below,

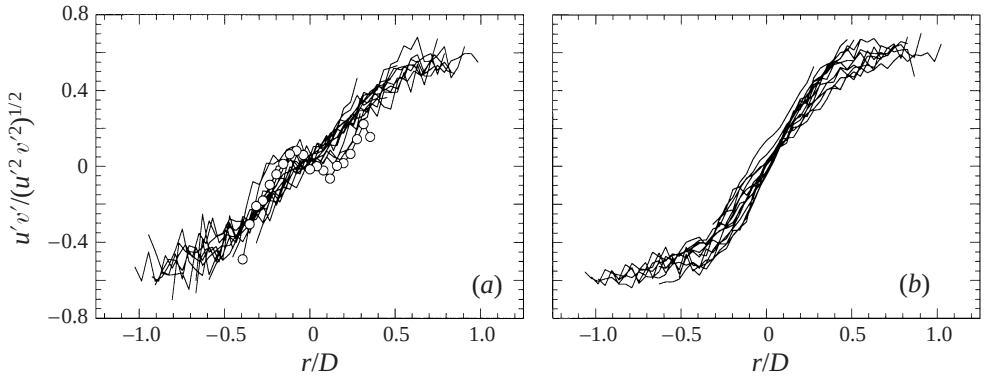

FIGURE 4. Radial scans of the gas velocity correlation in spray flames I (*a*) and II (*b*). The line with symbols is profile $z = 1.0D$.

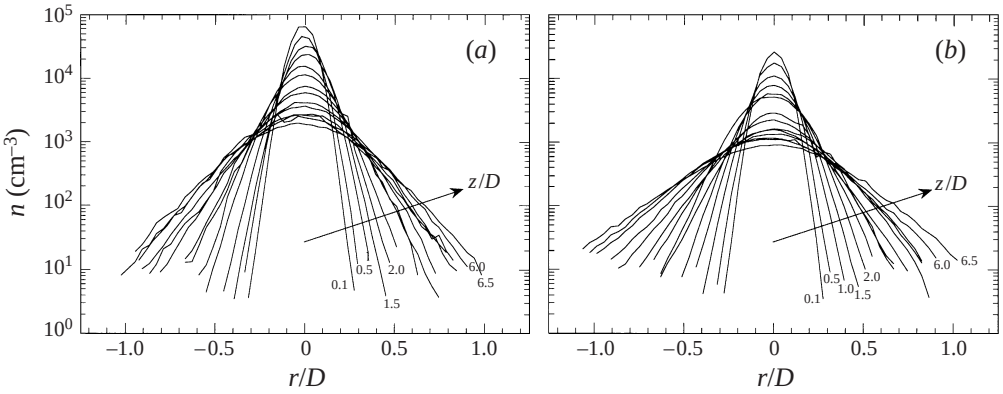

FIGURE 5. Radial scans of the drop number density in spray flames I (*a*) and II (*b*).

the gas phase quickly recovers from this dip on the centreline by accelerating as a result of the vaporization-induced momentum source. The effect is more pronounced in flame I, as expected, in view of the larger overall equivalence ratio, corresponding to higher mass loading and higher average drop number density. The correlation $\overline{u'v'}$ is presented in figure 4, non-dimensionalized by the local r.m.s values of both velocities, u' and v'. The collapse of the profiles is somewhat deceptive, because of the scatter in the measurement of this second-order quantity. At the first few axial positions and very close to the centreline ($z \leqslant 1.5D$), the velocity fluctuations are anti-correlated for positive r. One of these profiles ($z = 1.0D$) is drawn with symbols and line, in order to visualize this behaviour. The profiles further downstream show a linear behaviour with respect to r, as typical of axisymmetric jet flows (Pai 1954). The increase in the level of correlation is almost always monotonic, most likely because of the lack of data in the outer periphery of the flow field.

The droplet number density profiles are shown in figure 5. The data present a variation of two orders of magnitude in this variable along the spray centreline of each flame and anywhere between two to four orders of magnitude across the radial scans. This fact, coupled with the large droplet densities achieved at the centreline close to the exit, makes this type of spray flame well-suited for studies of group combustion under turbulent conditions. The data are consistent with the picture of

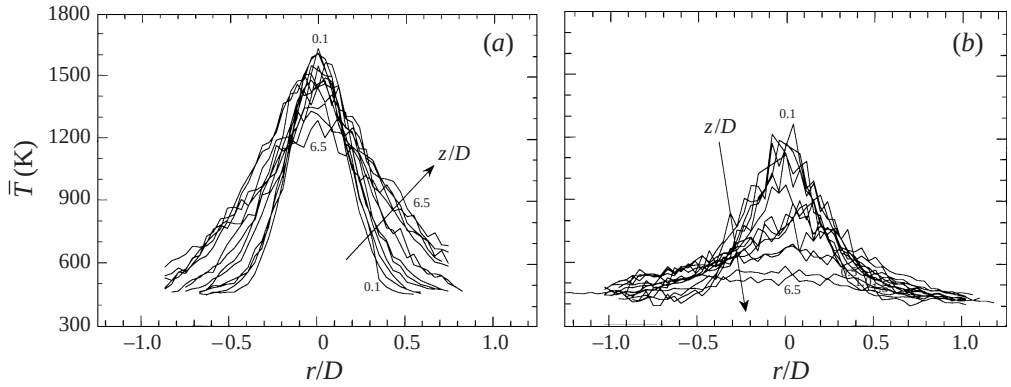

FIGURE 6. Radial scans of the average gas temperature in spray flames I (*a*) and II (*b*).

a spray flame spreading in the radial direction, with the fuel droplet number density decreasing along the axial position because of the spreading of the jet, as well as the concurrent droplet vaporization and eventual disappearance.

The measurements of the average gas temperature are shown in figure 6. Even though temperatures below 500–600 K are not accurately measured, we plot all data in figure 6, so as to bring forth at least the qualitative features of the whole temperature profiles in the spray flame. All the profiles are bell-shaped, with the maximum temperature at the exit ($\approx$ 1650 K for flame I and $\approx$ 1200 K for flame II) and decreasing slowly in the axial direction. Two points are immediately evident from this plot. First, the combustion temperatures are relatively low, which can be attributed to the low energetic content of methanol, or, insofar as the measured temperatures are lower than the adiabatic flame temperature, to the dynamics of the turbulent flow. Secondly, the maximum temperature at the exit is invariably encountered along the centreline. Experiments in laminar sprays (e.g. Chen & Gomez 1996), as well as in turbulent gaseous flames (e.g. Becker & Yamazaki 1978) usually show this trend only far from the burner exit, in the far field of the flame. The high temperatures measured close to the injector exit, at the positions with the highest liquid loading, are probably an artifact of the measurement technique. The diagnostic requirement of the absence of drops in the probe volume results in measurement bias in the high number density regions. In fact, it is conceivable that absence of drops could correspond to the rare passage of a flamelet through the axis, which, of course, would give an artificially high temperature measurement. It should be noted that such a heavy conditioning takes place at very few measurement positions and, hence, potential errors in these areas would have very small effects in what follows.

The velocity statistics of the dispersed phase comprise a large portion of the experimental results. For the purposes of the subsequent analysis, that concentrates on the mean field properties of the gas phase, the details of the size-classified measurements are rather unimportant, and only the mean field properties of the spray as a whole need be considered. Nevertheless, some consideration of the detailed droplet statistics is worthwhile. Accordingly, in figure 7 we plot the size–velocity correlation and probability density function of droplet size at three axial positions (z/D = 0.1, 3.5, 6.5) along the centreline of spray flame I. The size–velocity correlation is shown in grey-scale images, with darker pixels denoting larger number counts. It is evident from these plots that close to the burner exit the droplet velocity is smaller than that of the gas, corresponding to the smaller size classes ($d < 8\,\mu$m). As distance

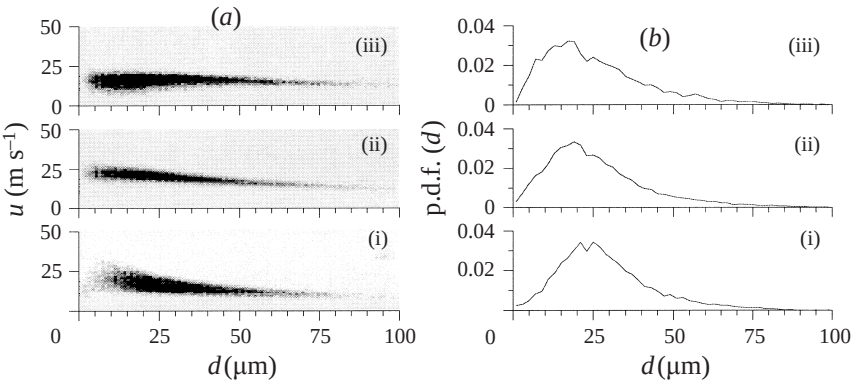

FIGURE 7. Droplet size–velocity correlation (*a*) and droplet probability size distributions (*b*) along the centreline of spray flame I, at $z = 0.1D$ (i), $z = 3.5D$ (ii) and $z = 6.5D$ (iii).

along the axis increases, the velocity difference is decreasing, and at the last axial position all drops move with similar velocities. The probability density functions show the behaviour expected in burning sprays, namely a shift of the distribution towards smaller values of droplet diameters due to combustion. At the same time, the spread of the distribution increases and its skewness becomes less positive, as a result of the faster vaporization rate of the smaller droplets. Significantly, both the correlations and the size distributions are mono-modal, suggesting that inter-droplet collisions are probably rare.

4. Theoretical premises

We now provide a theoretical framework and attempt to simplify this complex two-phase flow problem. Whenever possible, we will rely on the experimental measurements presented in the previous section, in order to limit the treatment to the essentials. The discussion will be restricted to the mass and momentum conservation equations for an axisymmetric turbulent spray flame. The hybrid experimental/theoretical approach will enable us to show that the density information, as inferred from the Raman thermometry, is adequate for a closed description of the spray flame, through suitable transformations. Using the experimental data, we shall also be able to evaluate a vaporization source term for the equations.

We shall start from the following form of the instantaneous mass and momentum governing equations for the gas phase:

$$\frac{\partial \rho}{\partial t} + \nabla \cdot \rho \boldsymbol{u} = n\dot{m}, \tag{4.1}$$

$$\frac{\partial \rho u}{\partial t} + \nabla \cdot \rho \boldsymbol{u} u - \frac{1}{r}\frac{\partial}{\partial r}\left(r\rho\nu\frac{\partial u}{\partial r}\right) = -n\dot{a} + n\dot{m}u_s, \tag{4.2}$$

in which the boundary layer approximation has been invoked, limiting the diffusion term to gradients in the radial (r) direction only. The flame is assumed isobaric, hence the radial momentum equation becomes redundant in the boundary layer formulation and will not be discussed. Equation (4.2) is written for the case of 'two-way coupling' of momentum, i.e. with the source terms that appear on the right-hand side because of the presence of the dispersed phase. Buoyancy was neglected in all the derivations

in the present work, since the Froude number ($Fr = U^2/gh$) based on the observed flame height h was larger than 50.

The source term $n\dot{m}$ appears in the continuity as an instantaneous field source of vapour, as proposed in Labowsky & Rosner (1978) and Chiu, Kim & Croke (1982). Writing the source as the combination of the droplet number density n with the single-drop vaporization term $\dot{m}$, amounts to an assumption of negligible corrections to the vaporization term because of drop proximity. It should be noted that even in the regions of highest loading, the inter-droplet spacing is at least 250 μm, which is equal to the minimum inter-droplet distance that produces collective effects in combusting drop arrays (Umemura 1994). Hence, the assumption of no proximity effects in the collective vaporization source term is valid everywhere except in the densest areas of our spray flames.

Two source terms appear in the gas momentum equation, coupling it with the spray momentum equation (not written here). One is due to the inter-phase drag, written as a combination of the drop number density n and the drag exerted by a single drop $\dot{a}$. The second source term corresponds to the momentum added to the gas because of the vaporization source $n\dot{m}$. Both terms involve the spray velocity u_s, as will be shown later.

The above equations can be written as

$$\frac{\partial r\rho}{\partial t} + \frac{\partial (r\rho u)}{\partial x} + \frac{\partial (r\rho v)}{\partial r} = rn\dot{m}, \tag{4.3}$$

$$r\rho\frac{\partial u}{\partial t} + r\rho u\frac{\partial u}{\partial x} + r\rho v\frac{\partial u}{\partial r} - \frac{\partial}{\partial r}\left(r\rho v\frac{\partial u}{\partial r}\right) + rn\dot{m}u = -rn\dot{a} + rn\dot{m}u_s. \tag{4.4}$$

The axial coordinate x, unlike the physical coordinate z (figures 3–6) that was measured from the burner exit, is measured from a 'virtual origin' that will be evaluated later.

There is not a large disparity between species molecular weights, insofar as the major species (CH_3OH, O_2, N_2, CO_2 and H_2O) are concerned. Therefore, one can invoke a constant molecular weight approximation, which, in turn, allows the determination of the gas density from the gas temperature through the ideal gas equation of state†.

By Reynolds averaging we obtain equations for the average field values:

$$\frac{\partial (r\overline{\rho u})}{\partial x} + \frac{\partial (r\overline{\rho v})}{\partial r} = r\overline{n\dot{m}}, \tag{4.5}$$

$$r\overline{\rho u}\frac{\partial \overline{u}}{\partial x} + r\overline{\rho v}\frac{\partial \overline{u}}{\partial r} + \frac{\partial}{\partial r}(r\overline{\rho u'v'}) + r\overline{n\dot{m}u} = -r\overline{n\dot{a}} + r\overline{n\dot{m}u_s}, \tag{4.6}$$

where a quasi-steady-state approximation has been invoked and all correlations of third order and some of second order were assumed negligible. Additionally, the turbulent transport terms were assumed to be much larger than the laminar terms. To solve the above system of equations for the mean field, one should resort to Favre averaging, as proposed in Bilger (1975). This well-known approach 'absorbs'

† A complete description of the problem would require consideration of the energy equation and $N-1$ independent species conservation equations (where N is the number of chemical species). The resulting system of equations would be much more complex, because of the presence of nonlinear source terms associated with combustion, in all but the equation of the nitrogen mass fraction. The experimental information on the gas phase temperature allows us to disregard the energy equation, thereby simplifying the treatment drastically.

the density into the dependent variables. The reason for avoiding such a procedure is simply that the PDA is not a temperature/density sensitive instrument, therefore we do not have any experimental information on Favre-averaged first- and second-order velocities and correlations. Instead, we shall neglect all correlations between ρ,u, and v as well as between n, $\dot{m}$,u and n, $\dot{a}$,u_s, which amounts to implicitly performing Favre averaging. Neglecting the correlations $\overline{\rho' u'}$ and $\overline{\rho' v'}$ is a defensible necessity if one wishes to avoid modelling such terms (Kolbe & Kollman 1980) thus complicating the picture even further.

Equations (4.5) and (4.6) become

$$\frac{\partial(r\bar{\rho}\,\bar{u})}{\partial x} + \frac{\partial(r\bar{\rho}\,\bar{v})}{\partial r} = r\bar{n}\bar{\dot{m}}, \tag{4.7}$$

$$r\bar{\rho}\,\bar{u}\frac{\partial \bar{u}}{\partial x} + r\bar{\rho}\,\bar{v}\frac{\partial \bar{u}}{\partial r} + \frac{\partial}{\partial r}(r\overline{\rho u' v'}) + r\bar{n}\bar{\dot{m}}\bar{u} = -r\bar{n}\bar{\dot{a}} + r\bar{n}\bar{\dot{m}}\bar{u}_s. \tag{4.8}$$

The ensuing density-time-averaged equations are identical to the laminar flow equations under specific assumptions for the radial transport of momentum, namely a gradient transport model (Bilger 1989). This approach is a usual modelling step that will be avoided, at least for the moment, for the following reason: it would amount to an over-specification of the problem, since it forces the classic similarity solution of a turbulent axisymmetric jet (George 1989), the applicability of which is yet to be demonstrated for the case of a turbulent spray flame.

An alternative approach will be pursued here. Since the Raman thermometry provides the temperature and density, one can perform the Howarth transformation (Howarth 1948) on the equations above. This transform to a mass-weighted radial coordinate makes use of the experimentally determined gas densities and 'absorbs' the density into the independent variables. In so doing, we decouple the energy equation from the rest of the conservation laws and thus avoid solving it altogether.

The transformation maps the incompressible boundary layer into a constant-density boundary layer. It should be noted that the presence of the vapour source makes the boundary layer compressible, even though the density may be constant (Rosner 1986). The subscript (+) will refer to this transformed system at constant density ρ_+. The rules of the transformation are

$$x_+ \equiv x \qquad \bar{u}_+ \equiv \bar{u}, \tag{4.9}$$

$$r_+^2 \equiv 2\int_0^r (\bar{\rho}/\rho_+) r\,\mathrm{d}r, \quad \bar{v}_+ \equiv \frac{r}{r_+}\frac{\bar{\rho}}{\rho_+}\bar{v} + \frac{\bar{u}}{r_+\rho_+}\int_0^r \frac{\partial \bar{\rho}}{\partial x} r\,\mathrm{d}r. \tag{4.10}$$

The transformation (4.10) ensures conservation of mass between the two systems (Williams 1985). It should be already evident that the ρ_+ of the constant-density system is a free parameter, for which the standard reference state (1 atm, 298 K) may be chosen, that is $\rho_+ = \rho_o$. The Howarth transformation simplifies continuity in the new compressed system. The momentum equation, however, is not similarly simplified, unless an extra conservation law is postulated between the two systems. This was introduced first by Mager (1958) in planar turbulent boundary layers and conserves the turbulent inertia forces (terms proportional to $\overline{u'v'}$) between the two systems. A similar law (and the one that will be used here) was later used by Libby (1962) and Ting & Libby (1960) in the treatment of axisymmetric turbulent flames. It involves the moment of the turbulent forces between the two systems, namely

$$r\bar{\rho}\overline{u'v'}\bar{\rho} r\,\mathrm{d}r\,\mathrm{d}x \equiv r_+\rho_+\overline{u'_+ v'_+}\rho_+ r_+ \mathrm{d}r_+ \mathrm{d}x_+. \tag{4.11}$$

The Howarth–Mager transform converts the mass and momentum equations (4.7) and (4.8) into the new compressed system

$$\frac{\partial \overline{u}_+}{\partial x_+} + \frac{1}{r_+}\frac{\partial (r_+ \overline{v}_+)}{\partial r_+} = \frac{\overline{n}\overline{\dot{m}}D}{\overline{\rho}U} \equiv \bar{\dot{s}}_+, \tag{4.12}$$

$$r_+\overline{u}_+\frac{\partial \overline{u}_+}{\partial x_+} + r_+\overline{v}_+\frac{\partial \overline{u}_+}{\partial r_+} + \frac{\partial}{\partial r_+}(r_+\overline{u'_+v'_+}) + r_+\bar{\dot{s}}_+\overline{u}_+ = -\frac{r_+\overline{n}\overline{\dot{a}}D}{\overline{\rho}U^2} + \frac{r_+\overline{n}\overline{\dot{m}}\overline{u}_s D}{\overline{\rho}U^2}$$
$$\equiv -r_+\bar{\dot{f}}_+ + r_+\bar{\dot{s}}_+\overline{u}_{s+}. \tag{4.13}$$

The equations are considered non-dimensional, with lengths divided by the burner diameter D and velocities divided by an average cold-flow value based on the flow rate, that is $U=10\,\mathrm{m\,s^{-1}}$ and $U=14.4\,\mathrm{m\,s^{-1}}$ for flames I and II, respectively. Note that both mass and momentum equations (4.12) and (4.13) were written in such a way that the left-hand side of the equation corresponds to the conservative part, with sources appearing on the right-hand side.

The vapour source term $\bar{\dot{s}}_+$ will be discussed next. The drop number density $\overline{n}$ comes directly from experiment, while the vaporization rate of an individual droplet ($\overline{\dot{m}}$) is given by Williams (1985) as

$$\overline{\dot{m}} = 2\pi\lambda/c_p d_{10}\ln(1+B) = 2\pi(\rho D^l)d_{10}\ln(1+B), \tag{4.14}$$

where d_{10} is the arithmetic mean of the drop diameters, and the Lewis number has been taken as unity for simplicity. The Spalding number B can be assumed to be constant, under the assumption that the fuel vapour concentration around the droplet is far from saturation and the temperature variations across the spray are not too large. Because of the logarithmic dependence of the term, the variations in the source term $n\dot{m}$ come mostly from the very large variations of n. Thus, constancy of B as well as the neglect of the correlations between $\overline{n}$ and $\overline{\dot{m}}$ during Reynolds averaging seem justifiable. Implicit in the adoption of (4.14) is the assumption that no cooperative effect is taking place during vaporization, i.e. the drops are not sufficiently close to each other to influence their individual vaporization rates. Since the individual drops are smaller than the Kolmogorov length scale, the relevant diffusivity for vaporization is the laminar one. Hence the drops are assumed to be vaporizing in a local laminar environment within even the smallest eddy of the turbulent gas. For the temperature dependence of the laminar mass diffusivity a Sutherland model was assumed which results in the following dependence of the diffusivity on the density:

$$D^l = D^l_+(\rho_+/\rho)^{1.7} = \nu^l_+(\rho_+/\rho)^{1.7}, \tag{4.15}$$

where the Schmidt number has also been assumed unity.

Finally, the source term appearing in the transformed equation is

$$\bar{\dot{s}}_+ = \overline{n}\overline{\dot{m}}D/(\overline{\rho}U) = \overline{n}\,2\pi D^l d_{10}\ln(1+B)D/U, \tag{4.16}$$

where the term D/U comes from non-dimensionalizing the equations.

By analogy with vaporization rate, the average drag on a single drop in the spray can be written as

$$\bar{a} = 3\pi\rho\nu^l d_{10}(\overline{u}-\overline{u}_s), \tag{4.17}$$

where the correlation between droplet size and velocity has been neglected. The combined inter-phase drag due to the presence of a collection of drops would be

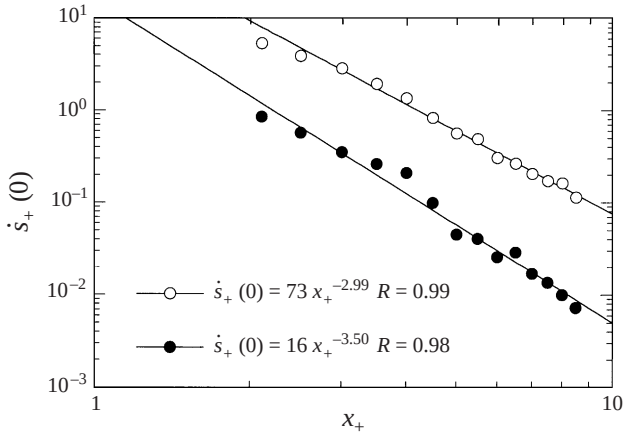

FIGURE 8. Vapour source similarity function in spray flames I (open symbols) and II (filled symbols). R is the coefficient of determination of the power-law fit.

accordingly

$$\bar{\dot{f}} = \bar{n}\bar{a} = \bar{n}\,3\pi\,\bar{\rho}v^l d_{10}(\bar{u} - \bar{u}_s), \tag{4.18}$$

where $\bar{u}_s$ is the average spray velocity, in the sense of volume-averaged field variable. As shown in Sadhal & Oguz (1985), the Stefan flow around the drop causes small deviations from the Stokes drag, which can be neglected. The form of the non-dimensional inter-phase drag appearing in the transformed equations then becomes

$$\bar{\dot{f}}_+ = \bar{\dot{f}}D/(\bar{\rho}U^2) = \bar{n}\,3\pi\,v^l d_{10}(\bar{u} - \bar{u}_s)D/U^2. \tag{4.19}$$

5. Similarity and implications

On the basis of the experimental information on gas density, we evaluate the transformed independent variables x_+ and r_+ corresponding to the physical coordinates x and r, using (4.10). Subsequently, self-similar behaviour is established for the vapour source $\dot{s}_+$ and the axial velocity u_+ in the spray flames. The velocity scaling is then contrasted to the classic solutions predicted for the incompressible gas jets, namely the inverse linear decay of axial velocity with axial distance (Schlichting 1987; Rosner 1986).

5.1. *Scaling of the vapour source*

In figure 8 we plot the values of the vapour source ($\dot{s}_+(0)$) along the centreline of the two spray flames. This variable can be described by a power law of x_+ along the centreline, with different exponents for the two flames. Specifically, we find $\dot{s}_+(0) \sim x_+^{-\alpha}$ with $\alpha = 3$ and 3.5 for flame I and II respectively. The axial distance x_+ is measured from the injector tip ($x_+ = z/D + 2$), since this is the position where the liquid drops are formed.

If we seek a similarity variable that produces collapse in the radial direction, we succeed by rescaling the radial coordinate as $\eta \equiv r_+/x_+^{\gamma}$ with $\gamma = 1.5$ and 1.75 for flame I and flame II respectively. This is shown in figure 9(a, b), where we plot the rescaled vapour source ($f_1(\eta) = x_+^{\alpha}\dot{s}_+$) against the similarity variable (η) for radial scans at $z > 1D$. There is evident collapse, which could be extended to all profiles, i.e. including the ones for $z \leqslant 1D$, by small adjustments of the position of the virtual

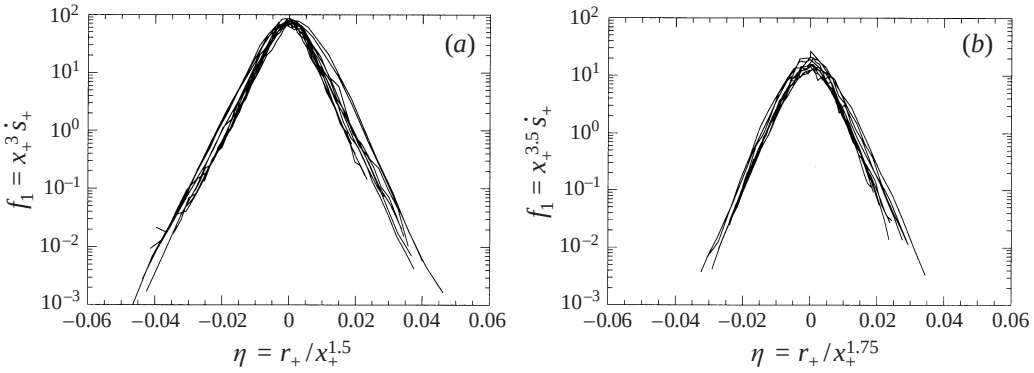

FIGURE 9. Radial behaviour of vapour source in spray flames I (*a*) and II (*b*). Data from radial scans $z = 1$–$6.5D$.

origin and the exponents γ and α. Such a procedure is rather tentative and will not be pursued here. The uncertainty in the temperature measurement in the most dense regions of the flame would affect the calculation of $\dot{s}_+$ in these areas, through changes in the laminar diffusivity (4.15). However, a possible error in temperature does not affect the determination of the power-law exponent significantly.

The implication of such a result is two-fold: first, we may describe the spray flame as a point source of vapour source. In what follows the less repetitive term 'point source of vaporization' will be used instead. Second, the exponent (γ) of axial distance in the similarity variable that effects the best collapse in figure 9(a, b) is half the exponent (α) of axial distance describing the centreline decay. This result, stemming from the experimental observation, can be rationalized as follows. The liquid mass conservation equation can be written in integral form as

$$(\partial/\partial x)\int_0^\infty r\rho_s u_s \,\mathrm{d}r = -\int_0^\infty rn\dot{m}\,\mathrm{d}r \sim -\int_0^\infty r_+\dot{s}_+\,\mathrm{d}r_+ = -x_+^{2\gamma-\alpha}\int_0^\infty \eta f_1(\eta)\,\mathrm{d}\eta, \quad (5.1)$$

where ρ_s and u_s are the density and axial velocity of the spray (Williams 1985), and the integral on the left-hand side of (5.1) is the total liquid flow rate as a function of x_+. On the basis of the high number density and temperature close to the exit, we expect the vaporization to be higher for smaller x_+, hence $2\gamma - \alpha \leqslant 0$. The requirement of finite liquid flow rate at $x_+ = 0$ excludes all cases of $2\gamma - \alpha < 0$ and enforces the condition $2\gamma = \alpha$, in agreement with the scaling of figure 9. This development implies that the combination of a point source of vaporization with finite liquid flow rate at the exit forces a linear decrease of liquid flow rate with axial distance.

5.2. *Scaling of the axial velocity*

In figures 10(a) and 10(b) we plot the centreline axial velocity $u_+(0)$, normalized by the cold flow velocity U, as measured by the PDA (dropping the overbars for notational simplicity) versus the independent variable x_+ for flames I and II respectively. In the same figures the values of the average spray velocity along the centreline are presented (similarly normalized). For the first half of the field of measurements, the gas velocity shows an increase with axial distance. In view of the rather small differences in gas density, as evidenced by the small decrease in temperature along the centreline, this behaviour must be explained by the competition of the source terms appearing in the momentum equation. In fact, the spray velocity along the centreline is smaller than the gas velocity and the inter-phase drag leads to deceleration of the gas. Hence, the

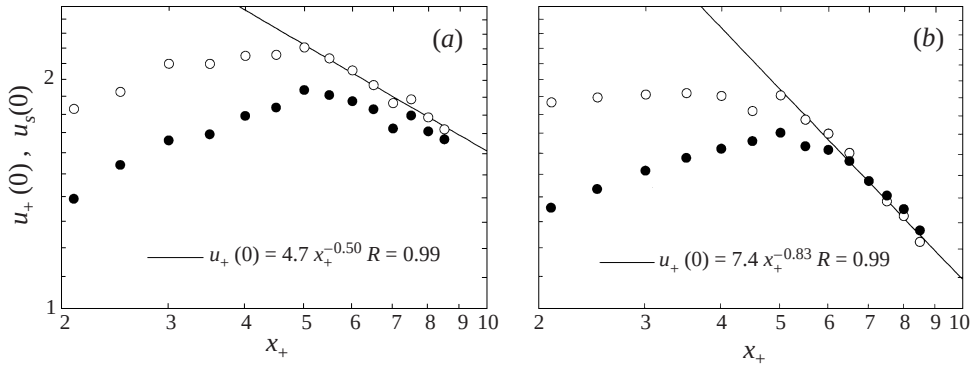

FIGURE 10. Centreline behaviour of gas and spray axial velocities (open and filled symbols respectively) in spray flames I (*a*) and II (*b*). R is the coefficient of determination of the power-law fit.

observed gas acceleration has to be an effect of the momentum addition through the spray vaporization. This is a clear example of the two-way coupling of momentum in the spray flames. Close to the burner exit, where the liquid loading is highest, and the velocity profiles exhibit the largest depression near the centreline (see also figure 3), acceleration prevails. The actual values of the exit velocity are lower for flame I as compared to flame II, and the subsequent acceleration is higher in flame I, both effects being attributable to the higher loading in this flame.

In the second half of the measurements, the axial velocity shows the expected decrease with axial distance, since the vaporization and heat release are less pronounced there and the jet spreading predominates. Thus, while in the lower portion of the flame two-way coupling of momentum is established, in the upper portion of the flame, one-way coupling of momentum (from the gas to the drops) is expected because of the decreasing number density of the liquid drops.

It is instructive to examine the integral form of the gas momentum equation, in order to further investigate the relative importance of the source terms. Integration along the radial direction (r) gives

$$\frac{\partial}{\partial x}\int_0^\infty 2\pi r\rho u^2\,\mathrm{d}r = -\int_0^\infty 2\pi r n\dot{a}\,\mathrm{d}r + \int_0^\infty 2\pi r n\dot{m}u_s\,\mathrm{d}r. \tag{5.2}$$

This equation, with the right-hand side identically set to zero reduces to the well-known momentum conservation of single-phase non-buoyant jets. Equation (5.2) can be converted through the Howarth transform into the compressed system

$$\frac{\partial}{\partial x_+}\int_0^\infty r_+ u_+^2\,\mathrm{d}r_+ = -\int_0^\infty r_+\dot{f}_+\,\mathrm{d}r_+ + \int_0^\infty r_+\dot{s}_+ u_s+\,\mathrm{d}r_+, \tag{5.3}$$

where all quantities are non-dimensional. The source integrals can be evaluated from the experimental data, and they are presented in figure 11(*a*, *b*). It is evident from these plots that the momentum added to the gas by vaporization is always larger than the momentum lost to the drops through the inter-phase drag. Furthermore, the imbalance of the sources does not only hold along the centreline as shown previously, but extends to the full integral along the radial direction. Hence the total gas momentum is increasing along the spray flames. It is interesting to note that both source terms become smaller as axial distance increases. The term due to vaporization is decreasing through the expected decrease of the spray velocity along the centreline, while the inter-phase drag becomes smaller as an effect of the expected momentum

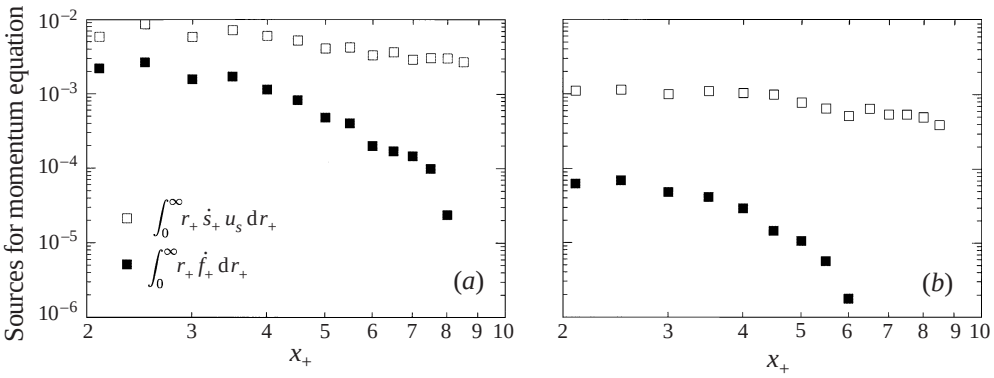

FIGURE 11. Centreline behaviour of momentum source terms in spray flames I (*a*) and II (*b*).

equilibration between the two phases (and, as is the case for the furthest positions of the measurements in figure 11, can change sign).

We expect that the combined effect of the increase of the left-hand-side of (5.3) and the decrease of the right-hand side would lead into a situation where the source terms are negligible compared to the momentum integral, hence an approximate conservation law would hold:

$$M = \int_0^\infty r\rho u^2 \, dr = \rho_+ \int_0^\infty r_+ u_+^2 \, dr_+ \approx \text{const}, \tag{5.4}$$

setting-up the case of 'one-way coupling' of momentum between the two phases. The lowest boundary of the region where one-way coupling of momentum holds in the spray flame, at least at the level of the mean axial velocity, will be assumed provisionally to coincide with the location where the centreline axial velocity starts decreasing with axial distance. We will seek a power-law behaviour of the axial velocity with respect to axial distance in this region. This nonlinear scaling is different from the linear behaviour of the (inverse) velocity with respect to axial distance ($u_+(0) \sim x_+^{-1}$) that is found in incompressible jets (Schlichting 1987) and jet flames (Dahm & Dibble 1992; Driscoll *et al.* 1996) and its justification will be presented subsequently.

If one sets the virtual origin of momentum at the injector tip, and hence assumes that $x_+ = z/D + 2$, the axial velocity shows a decrease proportional to (approximately) some fractional power of the axial distance. The best fit, as shown in figure 10 gives $u_+(0) \sim x_+^{-0.5}$ for flame I and $u_+(0) \sim x_+^{-0.83}$ for flame II, respectively. The positioning of the virtual origin at $z = -2D$ is somewhat arbitrary, yet a more accurate prediction is hindered by the fact that both the exponent of the velocity decay and the position of the virtual origin are unknown.

The behaviour in figure 10(*a*, *b*) suggests that similarity should be sought for the dependent variable $f_2(r_+, x_+) = u_+ x_+^\beta$, where β is the power-law exponent of the axial velocity decay. If one seeks similarity with respect to the simplest independent variable following a power law of the form $\xi = r_+/x_+^\beta$, then the following must hold:

$$M/\rho_+ = \int_0^\infty \frac{r_+}{x_+^{2\beta}} f_2^2(r_+, x_+) \, dr_+ = \int_0^\infty \frac{r_+}{x_+^\beta} f_2^2 \left(\frac{r_+}{x_+^\beta}, x_+ \right) d\frac{r_+}{x_+^\beta}$$
$$= \int_0^\infty \xi f_2^2(\xi, x_+) \, d\xi = \text{const.}, \tag{5.5}$$

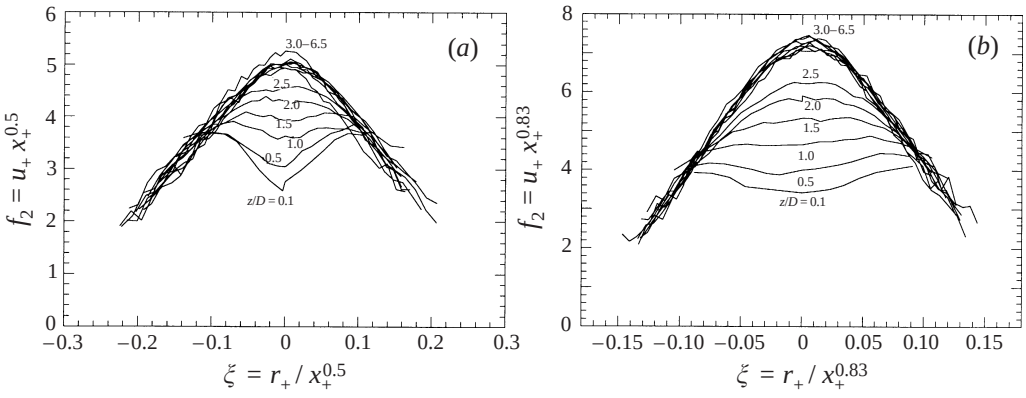

FIGURE 12. Axial gas velocity similarity function in spray flames I (*a*) and II (*b*).

where the approximate equation was converted to an exact relation. Then, constancy of the momentum flux in the spray (since there is no sink of momentum if two-way coupling is neglected) requires that the dependent variable f_2 be a function of ξ only, and hence

$$u_+ x_+^{\beta} = f_2(r_+/x_+^{\beta}), \tag{5.6}$$

i.e. the similarity variable $\xi = r_+/x_+^{\beta}$ is required by momentum conservation. This is corroborated by the experimental data, as shown in figure 12. There, we plot the radial scans of the rescaled axial velocity component $u_+x_+^{\beta}$ versus the independent variable $\xi \equiv r_+/x_+^{\beta}$, with numerical labels indicating the axial location of the scan (z/D). The first six profiles closest to the exit do not collapse, as expected, since the presence of high mass loading invalidates the form of the momentum conservation in (5.4). Further from the source, the good collapse of the data indicates that the above can indeed be a proper scaling of the axial momentum.

The presence of the drops has effects on the gas field at all possible orders (Faeth 1987). As shown in Parthasanarthy & Faeth (1990), the two-way coupling of momentum leads to gas turbulence modulation in homogeneous turbulence, even in stationary flows. Elghobashi & Truesdell (1993) showed that the dispersed phase has an effect even at the smallest scales of turbulence, yet on the level of mean quantities, the one-way coupling of momentum can be defined as the region where the momentum integral of (5.5) is constant, i.e. where there is on the average no net loss of gas momentum to the drops. Then, the assumption that one-way coupling prevails from the location where the axial velocity begins to decrease along the centreline (see figure 10) is well justified. Since the mass loading changes drastically within the spray flames, and in view of the expected effects of the drops on the gas phase, we may define the terms 'dense' or 'dilute' spray on the distinction between two-way coupling and one-way coupling of momentum on the level of mean velocity.

A crucial point for all the developments presented in this paper is the functional form of the self-similarity assumed to hold within the flow field. Equation (5.6), as well as the manner in which the axial velocity was plotted against axial distance in figure 10, both anticipate the possibility that the velocity behave as a power law of the axial distance. The exponent of that power law (β) turns out to be different from unity and dependent on the particular flame conditions, notably the overall stoichiometric coefficient Φ (see below).

The markedly different behaviour of the velocity decay along the spray centreline

Flame	$\dot{Q}_g$ (l min^{-1})	$\dot{m}_l$ (g min^{-1})	Φ	β
I′	66	5.1	0.42	0.26
I	80	5.1	0.35	0.50
II′	80	3.4	0.23	0.71
II	110	3.0	0.15	0.83

TABLE 1. Parameters of interest for the four spray flames studied along the centreline.

between the two flames prompted us to examine this behaviour in greater detail. Accordingly, the measurements of flames I and II were augmented by additional centreline velocity measurements that extended well beyond the visible tip of the spray flame. In addition, two more flames were studied in this fashion, for other combinations of air flow rate, $\dot{Q}_g$, and liquid mass flow rate, $\dot{m}_l$, and consequently Φ (table 1). All centreline measurements are presented in figure 13(*a–d*). We plot the inverse axial velocity, non-dimensionalized with respect to the mean gas velocity at the burner exit in each case (U). The dashed vertical bar shows the approximate average position of the visible tip of the spray flames, obtained from long-exposure digital photography.

Evident in these results is the existence of three different regions in the spray flames, as the dependence of axial velocity on axial coordinate changes. The initial region (A, drawn with diamonds) is where two-way coupling of momentum prevails, and where the velocity is increasing. In region (C), drawn with open circles, the flow field recovers the behaviour expected from single-phase jets and flames, namely a linear behaviour of inverse velocity with axial distance. The solid lines drawn through this region show the best linear fits and the existence of a virtual origin of momentum for this final region. An intermediate region (B) drawn with full circles is clearly visible, at least for the flames with higher liquid mass loadings. Although the beginning of this region can be fixed by momentum conservation, as done previously, its end cannot be as easily defined. One way would be to define it as the axial position where the velocity measurements depart appreciably from the linear scaling that holds in region (C).

A universal behaviour is perhaps expected for the final part of the flow field. This is not the case for the intermediate part (region B). As shown in figure 13, both types of scaling of axial velocity are in fact admissible, the dotted lines representing the best linear fit of inverse velocity in the intermediate region, the solid lines representing the nonlinear scaling. The former could describe the intermediate region as having different spreading rates and virtual origins for every flame, while the latter as it having different power-law exponents and the same virtual origin ($x_+ = 0$). As shown in George (1989), to admit either of the two scalings, the flow field must maintain a 'memory' of its initial conditions. In the case of spray flames the presence of the drops and the distributed source of vapour in the two-way coupling regions fulfils this condition.

It should be evident from the above that the experimental information alone is not sufficient for a decision between the two types of self-similar behaviour, mainly because of the limited extent of region B. Nevertheless, the nonlinear self-similarity presented here has clear advantages, at least in the case of spray flames. The linear scaling requires the introduction of a negative virtual origin, which would appear to be unphysical, if it is supposed to denote a length scale of the developing flow.

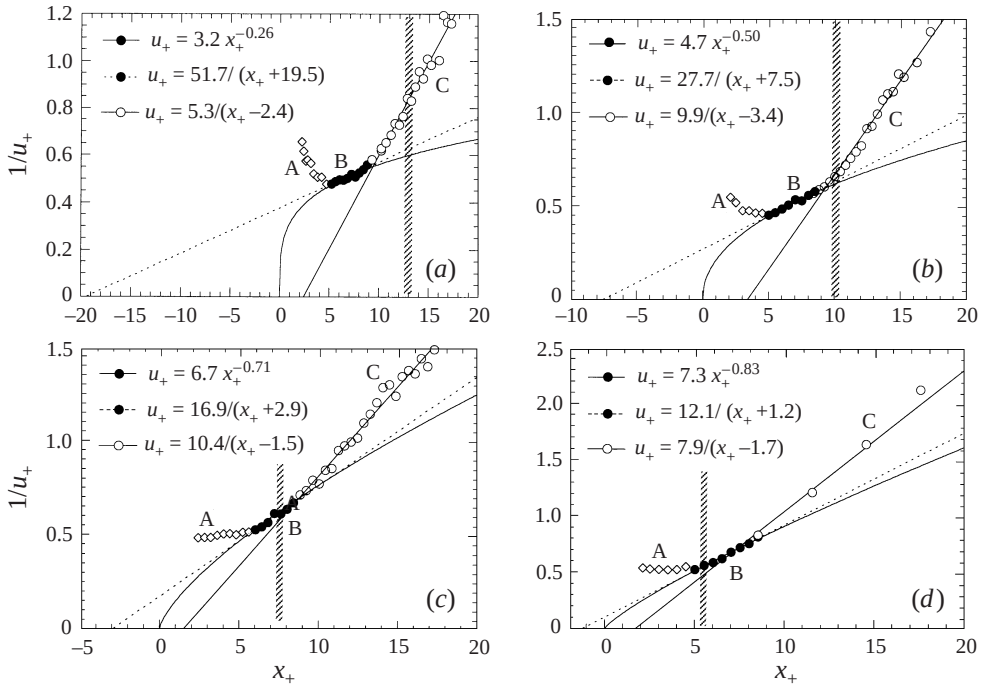

FIGURE 13. Centreline behaviour of inverse axial velocity in four different spray flames (see table 1): flame I′ (*a*), flame I (*b*), flame II′ (*c*), flame II (*d*). Three regions have been marked by different symbols: diamonds (A), filled circles (B), and open circles (C).

The argument is strengthened when one realizes that in the case of the flame with the highest Φ, presented in figure 13(*a*), the virtual origin required for universal self-similarity would be $x_+ \approx -19.5$, i.e. larger than the actual flame itself, as well as negative. On the other hand, the virtual origin for the nonlinear scaling that was presented here could be set on the injector exit for all flames, corresponding exactly at the initial point of the flow field.

The flame tip varies in position from the third region (figure 13*a*) to the beginning of the intermediate region (figure 13*d*). At the same time, the temperature measurements of flame II show the intermediate region forming in relatively cold, non-combusting areas of the flow field. These findings suggest that the appearance of the intermediate scaling of the axial velocity is not related to the heat addition due to combustion, but rather is a peculiar feature of spray flames, due to the presence of the two-way coupling (region A) and the vapour source.

Going back to the intermediate region for which self-similarity was established, and combining the experimental data from figures 8–12, we conclude that there exists scaling of the form

$$\dot{s}_+ x_+^{\alpha} = f_1\left(\frac{r_+}{x_+^{\gamma}}\right) = f_1(\eta), \quad u_+ x_+^{\beta} = f_2\left(\frac{r_+}{x_+^{\beta}}\right) = f_2(\xi). \tag{5.7}$$

The trend of increasing exponent β with increasing gas flow rate and decreasing liquid loading has been shown for four different flames in figure 13. Since the ratio of the two is proportional to the overall stoichiometric parameter Φ, we may cast the above trend in terms of Φ, namely a decrease in Φ results in an increase in β, as is

evident from table 1. As the liquid loading decreases between flames I′ and II, the effect of the two-way coupling becomes less pronounced, since the relative importance of the momentum source term is reduced, on account of the expected decrease in number density n and the decrease in the overall temperature in the spray flame (as already evidenced in the comparison between flames I and II). In accordance with the picture offered thus far, the intermediate region of the velocity scaling becomes less pronounced as Φ decreases. The exponent β increases towards unity, and in fact the two descriptions of velocity decay in region B are very similar. Furthermore, neither is all that different from the final inverse linear decay of region C, making the demarkation of the three regions less clear. Considering that as the liquid loading becomes smaller the flame length diminishes, one should expect to recover precisely such a behaviour of gas jets.

The scaling (5.7) is valid away from the singular point of the point source of momentum and vaporization ($x_+ = 0$) and hence the derived similarities are both asymptotic in the sense of Barenblatt (1996). A more elaborate approach would take the size as well as the strength of the sources into account, and consider the interphase terms in the momentum equation (two-way coupling). This would produce a description valid throughout the field of measurements. Such an approach would be more complex and will not be pursued here.

It should be noted that the self-similarity shown above is global, since the velocity in (5.7) is normalized with the exit velocity U and the local r_+ and x_+ by the exit diameter D. Then, a weaker form of local similarity necessarily holds in this case. If we define the radial position b_+ as the position where the local axial velocity is half the local velocity at the centreline ($u_+(0)$) and normalize the local axial velocity by the centreline value, then the following is the form of the local self-similarity:

$$u_+ b_+ = f_2\left(\frac{r_+}{b_+}\right). \tag{5.8}$$

The above is a necessary (but not sufficient condition) for (5.7) to hold. They become equivalent when one realizes that the growth rate b_+ is proportional to x_+^{β}. Even though the data from both flames show this trend in growth rate versus axial distance, these results will not be presented here, since, in effect, they can be trivially derived from the scaling presented above and the good collapse shown in figure 12(a, b) guarantees that a relationship of the form $b_+ = cx_+^{\beta}$ holds. Dahm & Dibble (1992) have postulated a similar form of local self-similarity to hold in gaseous jet diffusion flames. Following an argument substantially different from the one presented here, they also allow for the possibility of a global self-similar behaviour with an exponent β less than unity (see also Driscoll *et al.* 1996).

6. Reynolds stresses in turbulent spray flames

Next, the scaling of (5.7) will be used in the mass and momentum equations. Starting with (4.13), we can solve for the second-order correlation $\overline{u'_+ v'_+}$, if we first solve the mass conservation equation (4.12) for the radial velocity v_+. Combining (4.12) and (5.7) we get

$$r_+ v_+ = \frac{\beta}{x_+^{1-\beta}}\left(\xi^2 f_2 - \int_0^{\xi} \xi f_2 \,\mathrm{d}\xi\right) + \frac{1}{x_+^{\alpha-2\gamma}} \int_0^{\eta} \eta f_1 \,\mathrm{d}\eta. \tag{6.1}$$

By combining equations (4.13),(5.7) and (6.1) we arrive at

$$r_+\overline{u'_+v'_+} = \frac{f_2}{x_+^{\beta}}\left(\frac{\beta}{x_+^{1-\beta}}\int_0^{\xi}\xi f_2\,\mathrm{d}\xi - \frac{1}{x_+^{\alpha-2\gamma}}\int_0^{\eta}\eta f_1\,\mathrm{d}\eta\right). \tag{6.2}$$

Both (6.1) and (6.2) offer predictions for the radial velocity and the Reynolds stress. Unfortunately, the experimental information on v cannot be converted into v_+ through the Howarth–Mager transform, since the resolution of the Raman thermometry does not warrant any calculation of density gradients. We will instead concentrate on the prediction for the Reynolds stress in (6.2).

It is easy to verify that the two integrals contained on the right-hand side of (6.2) are both related to mass flux in the spray flame:

$$\int_0^{\xi}\xi f_2(\xi)\,\mathrm{d}\xi = \frac{1}{x_+^{\beta}}\int_0^{r_+} r_+u_+\,\mathrm{d}r_+ = \frac{1}{\rho_+x^{\beta}}\int_0^{r} r\rho u\,\mathrm{d}r \tag{6.3}$$

$$\int_0^{\eta}\eta f_1(\eta)\,\mathrm{d}\eta = \frac{1}{x_+^{2\gamma-\alpha}}\int_0^{r_+} r_+\dot{s}_+\,\mathrm{d}r_+ = \frac{1}{\rho_+x_+^{2\gamma-\alpha}}\int_0^{r} rn\dot{m}\,\mathrm{d}r. \tag{6.4}$$

The first integral (6.3) is related to the fractional mass entrainment from the ambient, while the second integral (6.4) is the fractional vapour production in the spray. The first term tends to increase the value of the correlations $\overline{u'_+v'_+}$, and is related to the turbulent transport of momentum through the spray flame. The second term tends to reduce the value of the correlation, working *against* turbulent transport. Since this term arises because of the presence of the vapour source, it can be construed as a relaminarization tendency due to vaporization.

The practical importance of the self-similarity of the axial velocity can be seen in the first integral (6.3). The fact that the velocity scales with an exponent β smaller than unity leads to smaller entrainment of the ambient air than for a flow corresponding to $\beta = 1$. The intermediate region of the flow identified above can be a significant portion of the flame before extinction. The fact that this exponent can become much smaller than unity, as in the flame of figure 13(*a*), means that in practical cases of spray flames the air entrainment can be much smaller than expected from the naive application of single-phase jet laws.

We may now proceed to the actual comparison between the experimental data and the prediction of the values of correlation $\overline{u'_+v'_+}$ in (6.2). For conciseness we present the experimental data only from flame I. Figure 14 shows the correlation (solid line), calculated from the right-hand side of equation (6.2) and the experimental data (circles), both plotted versus radial distance r_+. The agreement is good downstream of the exit (for $z \geqslant 3$) where the similarity scaling of the velocity holds, and becomes even better further downstream, where one of the two terms, specifically the reduction due to the vaporization, becomes negligible. Note that no simple scaling may exist for the correlations since the two integrals that comprise it are functions of different similarity variables, namely ξ and η. Similar results have been obtained from flame II. The agreement in that case is made worse at the last couple of radial scans (for $z > 5.5D$). This can be attributed to the experimental over-prediction of the temperature at the sides of the spray flame, leading to errors in the calculation of r_+ and hence to the integrals in (6.2). This is also the likely reason for the small departures at the sides of the spray flame I shown in figure 14, even when the profiles show very good agreement everywhere else.

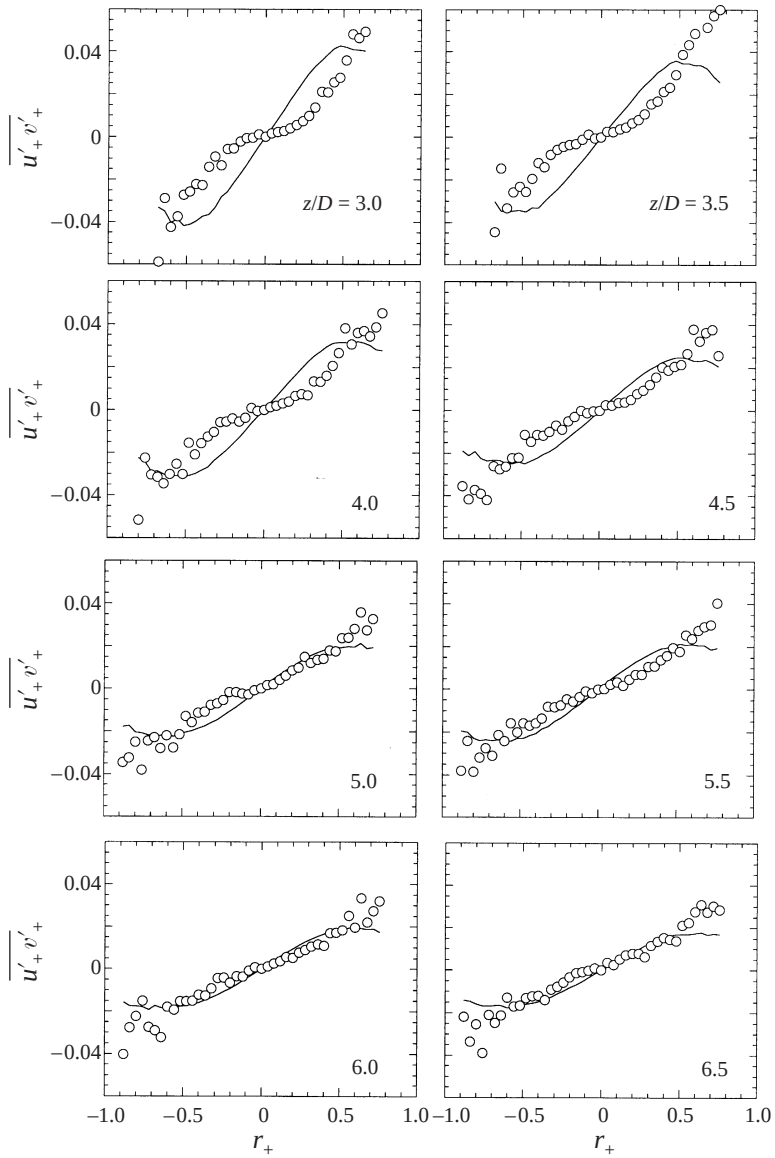

FIGURE 14. Reynolds stess term at various axial locations in flame I. Solid line calculated from equation (6.2). Symbols correspond to experimental measurements.

7. Closure and modelling

Closure of the turbulent boundary layer equations can be brought about with a simple scalar model of the turbulent transport, such as a gradient transport model. As a result, first, a simple constant, inaccurate though it may be, quantifies the extent of the turbulent transport. Second, first-order quantities can be solved for. This strategy appears to be justified in the present case as a first approach to the relatively unexplored area of turbulent spray combustion. More sophisticated models will be pursued in the future.

From the form of the term $\overline{u'_+ v'_+}$ in (6.2), it is obvious that a gradient transport

model with a constant turbulent diffusivity is not applicable in this case†, since the term $\overline{u'_+v'_+}$ is manifestly proportional to the axial velocity u_+. If we split the term into the two contributions mentioned above, namely one due to the transport and one due to the vaporization, we may try a simple model for the part related to turbulent transport. Accordingly, we define

$$\overline{u'_+v'_+}|_t \equiv \frac{\beta u_+}{r_+ x_+^{1-\beta}} \int_0^\xi \xi f_2 \, \mathrm{d}\xi. \tag{7.1}$$

We will use the classic approach of a mixing length. As can be seen in Pai (1954), the mixing length is a scalar that allows for local similarity of the Reynolds stresses, under the condition of constant transport coefficient throughout the flow field. We will attempt to satisfy the local self-similarity by normalizing the stess terms by $u_+^2(0)$, velocities by $u_+(0)$ and lengths by b_+, i.e. the local parameters of the flow. Then, an effective turbulent diffusivity v_t should relate these terms via

$$\frac{\overline{u'_+v'_+}|_t}{u_+^2(0)} = -v_t \frac{\partial(u_+/u_+(0))}{\partial(r_+/b_+)}. \tag{7.2}$$

Assuming $b_+ = cx_+^\beta$ and substituting (7.2) into (7.1) we get

$$-c\, v_t\, x_+^{1-\beta}/\beta = (f_2/\xi f_2') \int_0^\xi \xi(f_2/f_2(0))\, \mathrm{d}\xi, \tag{7.3}$$

where the prime denotes differentiation with respect to ξ. Since the right-hand side of the equation is a function of ξ, the effective turbulent diffusivity cannot be constant throughout the flow field, except (and only) when $\beta = 1$. This is a result that was first proven by George (1989) but has had, so far, no practical repercussions. The simple scaling of (7.2) forces the scaling of the effective diffusivity

$$-cv_t\, x_+^{1-\beta}/\beta = (\check{f}_2/\xi \check{f}'_2) \int_0^\xi \xi \check{f}_2 \, \mathrm{d}\xi \equiv -\lambda(\xi). \tag{7.4}$$

Of course, there is a way of 'rescuing' the local self-similarity of the Reynolds stresses by requiring $\lambda(\xi)$ to be a constant. Then, the effective diffusivity v_t is not constant, rather it varies as $x_+^{\beta-1}$. The experimental data can provide a check on that assumption as shown in figure 15, where we plot $\lambda(\xi)$ as calculated from (7.4), using the data from flame I. The data shows the collapse of $\lambda(\xi)$ to a constant for the profiles of the intermediate region, where self-similarity of the velocity holds. Exceptions close to the centreline ($\xi = 0$) are probably due to numerical errors, namely divisions by small numbers. It is worth noting that the data from flame II (not presented here) show a similar behaviour. A different value of the constant λ characterizes flame II, signifying that $\lambda(\xi)$ can be constant within a spray flame but need not be constant between different spray flames.

The mixing-length arguments above constitute closure of the problem at the first moment. We can solve for the axial velocity similarity profile $f_2(\xi)$. Equation (7.3)

† Despite that fact, we used such an assumption as a crude means of validating the hypothesis of negligible laminar transport in (4.6). We calculated an effective turbulent diffusivity from the measurements of $\overline{u'_+v'_+}$ and the profiles of $\overline{u}_+$ and contrasted it to the laminar diffusivity at the highest temperature. The turbulent quantity was always at least an order of magnitude larger than the laminar one, thus substantiating the assumption of the prevalence of turbulent transport.

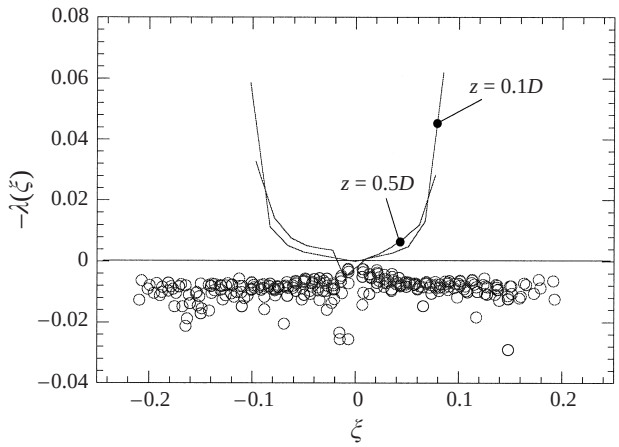

FIGURE 15. Gradient modelling of the turbulent stress term. Solid lines correspond to profiles at the exit ($z = 0.1D$, $0.5D$); circles denote λ far from the exit ($z > 3D$). All data from flame I.

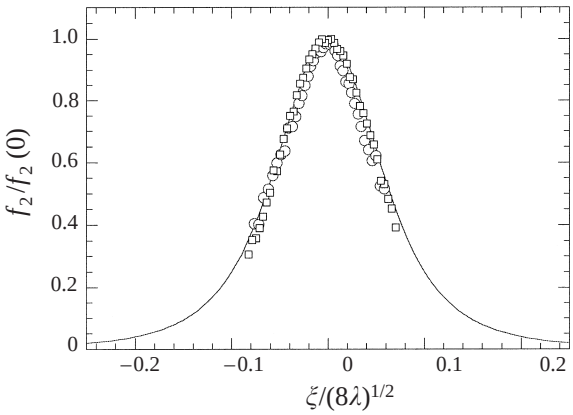

FIGURE 16. Comparison between the similarity function $\check{f}_2$ computed from equation (7.7) (solid line) and measured at axial position $z = 5D$ in flame I (circles) and II (squares).

leads to

$$\lambda = -(\check{f}_2/\xi\check{f}_2') \int_0^{\xi} \xi\check{f}_2 \, \mathrm{d}\xi, \tag{7.5}$$

where $\check{f}_2$ denotes the normalization $f_2(\xi)/f_2(0)$. Under the substitution $\check{f}_2 = \mathrm{e}^y$ this leads to the equation

$$\xi y' + \xi^2 y'' + \xi^2 \mathrm{e}^y/\lambda = 0. \tag{7.6}$$

The above has been solved analytically (and verified numerically) as

$$\check{f}_2 = (1 + \xi^2/8\lambda)^{-2}. \tag{7.7}$$

The result in (7.7) can be checked against the experiments, thus validating the whole procedure. Since the profiles of f_2 (and hence $\check{f}_2$) show a reasonable collapse in the intermediate region of the flame (figure 12), for clarity of presentation it will suffice to compare a typical experimental profile (from $z = 5.0$) to the solution of equation (7.7), as shown in figure 16. The similarity functions from both flames are

plotted in this figure, as an indication that the calculated profile of $\check{f}_2$ appears to be 'universal', when the proper value of λ is taken into account. The agreement is very good, yet the significance of such a result is somewhat limited by the elementary means of effecting closure, i.e. the mixing length approach. Nevertheless, this model should be useful as a first approach to the problem at hand.

8. Conclusions

An experimental study was performed on two turbulent spray flames in which the droplets were introduced in the gas at small velocity relative to the gas phase to minimize the liquid injector effect on the spray behaviour. Applications of Phase-Doppler interferometric techniques and of Stokes/anti-Stokes Raman thermometry enabled us to measure the size, velocity and concentration of the droplets, as well as the gaseous velocity and temperature. A hybrid experimental/theoretical approach, relying on the experimental measurements and on appropriately transformed continuity and momentum equations, led to the following principal conclusions:

(1) The spray flame can be divided into three different regions, based on the behaviour of axial velocity along the centreline. In the first region, close to the burner, two-way coupling of momentum dominates. In the intermediate region, the axial velocity along the centreline follows a fractional power law of the distance from a virtual origin. This finding can be contrasted with the behaviour of incompressible turbulent jets that are characterized by an inverse first-power dependence on the same parameter. Such a dependence is recovered in the third and last portion of the spray flames. The implication is that the entrainment rate of these spray flames is drastically different from that of their incompressible counterparts;

(2) The source term in the continuity equation, that is modelled neglecting droplet interactive effects, decays along the centreline as an inverse power of the distance from the virtual origin;

(3) Self-similar behaviour for both variables, axial velocity and vapour source terms, was found throughout the spray flame, in both flames that were studied in detail. In the case of the axial velocity, self-similarity does not apply near the burner exit, partly because of two-way coupling between droplets and the gaseous stream;

(4) By using the derived scaling laws, an expression for the Reynolds stress term in the momentum equation was inferred, accounting for two competing contributions. One term tends to increase the value of the velocity correlation, is related to the cumulative mass entrainment and can be interpreted as the contribution of the turbulent momentum transport. The second term reduces the value of the velocity correlation, working against turbulent transport. Such a term arises because of the presence of the vapour source and can be construed as a tendency towards relaminarization induced by vaporization;

(5) Modelling of the turbulent momentum transport term of the Reynolds stress, to bring about closure in terms of a mixing-length-like scalar, the average axial velocity and its gradient, yielded good agreement with the experimental measurements.

The authors would like to thank Professors F. A. Williams (UC San Diego) and Amable Liñán (Universidad Politécnica de Madrid) for helpful suggestions. The support of NASA, under the Microgravity Science and Applications Program, Grant NAG3-1688, and of NSF, through a NSF Young Investigator Award to one of the authors (A. G.), and Equipment Grant # CTS-9112601, is gratefully acknowledged.

REFERENCES

Barenblatt, G. I. 1996 *Scaling, Self-Similarity, and Intermediate Asymptotics*. Cambridge University Press.

Becker, H. A. & Yamazaki, S. 1978 Entrainment, momentum flux and temperature in vertical free turbulent diffusion flames. *Combust. Flame* **33**, 123–149.

Bilger, R. W. 1975 A note on Favre averaging in variable density flows. *Combust. Sci. Technol.* **11**, 215–217.

Bilger, R. W. 1989 Turbulent diffusion flames. *Ann. Rev. Fluid Mech.* **21**, 101–135.

Chang, R. K., Eickmans, J. H., Hsieh, W. F., Wood, C. F., Zhang, J. Z. & Zheng, J. B. 1988 Laser-induced breakdown in large transparent water drops. *Appl. Opt.* **27**, 2377–2385.

Chen, G. & Gomez, A. 1992 Counterflow diffusion flames of quasi-monodisperse electrostatic sprays. *Twenty-Fourth Symp. (Intl) on Combustion*, pp. 1531–1539. The Combustion Institute, Pittsburgh PA.

Chen, G. & Gomez, A. 1996 Co-flow laminar diffusion flames of monodisperse sprays: structure, evaporation and microgravity effects. *Combust. Sci. Technol.* **115**, 177–201.

Chen, G. & Gomez, A. 1997 Dilute laminar spray diffusion flames near the transition from group combustion to individual droplet burning. *Combust. Flame* **110**, 392–404.

Chigier, N. A. & McCreath, C. G. 1974 Combustion of droplets in sprays. *Acta Astro.* **1**, 687–710.

Chiu, H. H., Kim, H. Y. & Croke, E. J. 1982 Internal group combustion of liquid droplets. *19th Symp. (Intl) on Combustion,* pp. 971–980. The Combustion Institute, Pittsburgh, PA.

Dahm, D. J. A. & Dibble, R. W. 1992 Coflowing turbulent jet diffusion flame blowout. *Twenty-Second Symp. (Intl) on Combustion*, pp. 801–808. The Combustion Institute, Pittsburgh PA.

Driscoll, J. F., Huh, H., Yoon, Y. & Donbar, J. 1996 Measured lengths of supersonic hydrogen–air jet flames – compared to subsonic flame lengths – and analysis. *Combust. Flame* **107**, 176–186.

Eckbreth, A. C. 1988 *Laser Diagnostics for Combustion Temperature and Species*. Abacus.

Elghobashi, S. & Truesdell, G. C. 1993 On the two-way interaction between homogeneous turbulence and dispersed solid particles. I. Turbulence modulation. *Phys Fluids* A **5**, 1790–1801.

Faeth, G. M. 1987 Mixing, transport, and combustion in sprays. *Prog. Energy Combust. Sci.* **13**, 293–345.

Gao, L. P., D'Angelo, Y., Silverman, I., Gomez, A. & Smooke, M. D. 1996 Quantitative comparison of detailed numerical computations and experiments in counterflow spray diffusion flames. *Twenty-Sixth Symp. (Intl) on Combustion*, pp. 1739–1746. The Combustion Institute, Pittsburgh PA.

George, W. K. 1989 The self-preservation of turbulent flows and its relation to initial conditions and coherent structures. In *Advances in Turbulence* (ed. W. K. George & R. Arndt). Hemisphere.

Howarth, L. 1948 Concerning the effect of compressibility on laminar boundary layers and their separation. *Proc. R. Soc. Lond.* A **194**, 16–42.

Kamimoto, T. & Kobayashi, H. 1991 Combustion processes in diesel engines. *Prog. Energy Combust. Sci.* **17**, 163–189.

Karpetis, A. N. & Gomez, A. 1996 Temperature measurements in spray flames by spontaneous Raman scattering. *Opt. Lett.* **21**, 704–706.

Kolbe, W. & Kollmann, W. 1980 Prediction of turbulent diffusion flames with a four equation turbulence model. *Acta Astro.* **7**, 91–104.

Labowsky, M. & Rosner, D. E. 1978 'Group' combustion of droplets in fuel clouds. I. Quasi-steady predictions. *Evaporation–Combustion of Fuels.* Adv. Chem. Ser. (ed. J. T. Zung), No. 166, pp. 63–79. American Chemical Society.

Libby, P. A. 1962 Theoretical analysis of turbulent mixing of reactive gases with application to supersonic combustion of hydrogen. *Am. Rocket Soc. J.* **32**, 388–396.

Longmire, E. K. & Eaton, J. K. 1992 Structure of a particle-laden round jet. *J. Fluid Mech.* **236**, 217–257.

Luczak, A., Beushausen, V., Eisenberg, S., Knapp, M., Schlüter, H., Andresen, P., Malobabic, M. & Schmidt, A. 1996 New nonintrusive laser diagnostic tools for design and optimization of technically applied combustion systems. *Combust. Sci. Technol.* **116–117**, 541–566.

Mager, A. 1958 Transformation of the compressible turbulent boundary layer. *J. Aero. Sci.* **25**, 305–311.

Marchese, A. J., Dryer, F. L., Colantonio, R. O. & Nayagan, V. 1996 Microgravity combustion of methanol and methanol/water droplets: drop tower experiments and model predictions. *Twenty-sixth Symp. (Intl) on Combustion*, pp. 1209–1217. The Combustion Institute, Pittsburgh, PA.

McLaughlin, D. K. & Tiederman, W. G. 1973 Biasing correction for individual realization of laser anemometer measurements in turbulent flows. *Phys Fluids* **16**, 2082–2088.

O'Young, F. & Bilger, R. W. 1997 Scalar gradient and related quantities in turbulent premixed flames. *Combust. Flame*, **109**, 682–700.

Pai, Shih-I 1954 *Fluid Dynamics of Jets.* Van Nostrand.

Parthasanarthy, R. N. & Faeth, G. M. 1990 Turbulence modulation in homogeneous dilute particle-laden flows. *J. Fluid Mech.* **220**, 485–514.

Rosner, D. E. 1986 *Transport Processes in Chemically Reacting Flow Systems*, 2nd Edn. Butterworth–Heinemann.

Sadhal, S. S. & Oguz, H. N. 1985 Stokes flow past compound multiphase drops: the case of completely engulfed drops/bubbles. *J. Fluid Mech.* **160**, 511–529.

Schlichting, H. 1987 *Boundary-Layer Theory*, 7th Edn. McGraw-Hill.

Takahashi, F., Schmoll, W. J., Switzer, G. & Shouse, D. T. 1996 Structure of a spray flame stabilized on a production engine combustor cup. *Twenty-Fith Symp. (Intl) on Combustion*, pp. 183–191. The Combustion Institute, Pittsburgh PA.

Ting, L. & Libby, P. A. 1960 Remarks on the eddy viscosity in compressible mixing flows. *J. Aero. Sci.* **27**, 797–798.

Umemura, A. 1994 Interactive droplet vaporization and combustion: approach from asymptotics. *Prog. Energy Combust. Sci.* **20**, 325–372.

Williams, F. A. 1985 *Combustion Theory*, 2nd Edn. Benjamin/Cummings.